Applied Physics Letters

Implement quantum tomography of polarization-entangled states via nondiffractive metasurfaces

Cite as: Appl. Phys. Lett. **121**, 081703 (2022); https://doi.org/10.1063/5.0102539
Submitted: 10 June 2022 • Accepted: 01 August 2022 • Published Online: 24 August 2022

Zheng Wang, Yue Jiang, Ya-Jun Gao, et al.

AIP Publishing

Applied Physics Letters ARTICLE scitation.org/journal/apl

Implement quantum tomography of polarization-entangled states via nondiffractive metasurfaces

Cite as: Appl. Phys. Lett. **121**, 081703 (2022); doi: 10.1063/5.0102539
Submitted: 10 June 2022 · Accepted: 1 August 2022 ·
Published Online: 24 August 2022

Zheng Wang,[1] Yue Jiang,[1] Ya-Jun Gao,[1] Ren-Hao Fan,[1] Dong-Xiang Qi,[1] Rui Zhong,[1] Hu-Lin Zhang,[1] Ru-Wen Peng,[1,a)] and Mu Wang[1,2,a)]

AFFILIATIONS

[1]National Laboratory of Solid State Microstructures, School of Physics, and Collaborative Innovation Center of Advanced Microstructures, Nanjing University, Nanjing 210093, China
[2]American Physical Society, Ridge, New York 11961, USA

[a)]**Authors to whom correspondence should be addressed:** rwpeng@nju.edu.cn and muwang@nju.edu.cn

ABSTRACT

Traditional optical elements, such as waveplates and polarization beam splitters, are essential for quantum state tomography (QST). Yet, their bulky size and heavy weight are prejudicial for miniaturizing quantum information systems. Here, we introduce nondiffractive silicon metasurfaces with high transmission efficiency to replace the traditional optical elements for QST of polarization-entangled states. Two identical silicon metasurfaces are employed, and each metasurface comprises four independent districts on a micrometer scale. The unit cell of each district consists of two silicon nanopillars with different geometrical sizes and orientation angles, and the interference of the scattered waves from the nanopillars leads to a single output beam from the district with a specific polarization state with a transmission efficiency above 92%. When the two-photon polarization-entangled state shines on different districts of two metasurfaces, each photon of the photon pair interacts with the local nanopillars within the district, and the two-photon state is projected onto 16 polarization bases for state reconstruction. We experimentally demonstrate the reconstruction of four input Bell states with high fidelities. This approach significantly reduces the number of conventional optical components in the QST process and is inspiring for advancing quantum information technology.

Metasurfaces can effectively manipulate the amplitude, phase, polarization, wavefront shape, and propagation direction of light.[1–11] In these scenarios, polarization manipulation based on metasurface has already shown great potential for photonics applications.[12–20] One typical approach relies on Pancharatnam–Berry phase (PB phase) metasurfaces,[21–25] which tunes the polarization states by rotating the metastructures. Alternatively, by inflating/contracting geometrical sizes of the metastructures, the geometrical-scaling-induced (GSI) phase is applied,[26,27] and different polarization states can output in different directions simultaneously. Moreover, by assembling metastructures with varying angles of rotation and geometrical sizes, the distributions of output polarization states could be controlled.[28,29] Due to their excellent performance, metasurfaces have recently been applied in quantum regimes.[30–42] For example, an all-dielectric metasurface made of metagratings has demonstrated nonclassical multiphoton interference and state reconstruction at the subwavelength scale.[43] This significant progress indicates the feasibility of ultrathin quantum metadevices for manipulating and measuring multiphoton quantum states. Very recently, metasurfaces have shown remarkable capabilities in quantum entanglement,[44,45] quantum interference and modulation,[46–48] and quantum sensing and imaging.[49–52]

In multiphoton quantum optics, quantum state tomography (QST) characterizes the quantum state of a system through a series of complete projective measurements on different bases.[53–58] In the QST of the multiphoton polarization-entangled state, each photon passes through a combination of a quarter-wave plate (QWP), half-wave plate (HWP), and a polarization beam splitter (PBS) and is projected onto a specific polarization state.[59,60] By rotating the QWP and HWP, the multiphoton state is projected onto different polarization bases. Meanwhile, the multiphoton coincidence counts are measured. The density matrix can be reconstructed with the measured multiphoton coincidence counts by the maximum likelihood estimation algorithm.[53,61] According to the density matrix, some crucial parameters, such as fidelity, an index characterizing the proximity between the measured and ideal entangled state, etc., are extracted.[54,62] To replace the bulky optical elements in QST, people try an alternative approach

via three interleaved metagratings.[43] Each metagrating consists of nanopillars with varying geometrical sizes and angles and diffracts the input state into two elliptical polarization states propagating in two channels. In this way, six beam splitting channels are established. By analyzing the coincidence counts between the two output channels, this approach enables multiphoton tomography to reconstruct quantum states instead of depending on traditional waveplates and polarization beam splitters. However, the overall size of the metagratings remains on the millimeter scale ($2 \times 2\,\mathrm{mm}^2$). Most seriously, each metagrating diffracts only less than 30% of the incident energy to two output channels. Therefore, new approaches with more compact size and higher transmission efficiency are essential for the future development of miniaturizing photonic systems.

In this work, we realize QST of the polarization-entangled states based on two nondiffractive silicon metasurfaces with high transmission efficiency. Each metasurface comprises four independent districts constructed with silicon nanopillars, $350 \times 350\ \mu\mathrm{m}^2$ in size. The interference of the nanopillar radiations leads to one output with a linearly polarized (LP) or circularly polarized (CP) state. We can acquire the density matrix of the two-photon polarization-entangled state with two silicon metasurfaces. Specifically, by translating the metasurface with a three-axis translation stage, each photon of the input photon pair interacts with each district of every metasurface. The two-photon state is projected onto 16 (4×4) polarization bases, and 16 two-photon coincidence counts are measured. The density matrix is obtained by the maximum likelihood estimation algorithm via the measured coincidence counts. To prove this, we experimentally reconstruct the density matrices of four different input Bell states, $|\Psi^+\rangle$, $|\Psi^-\rangle$, $|\Phi^+\rangle$, and $|\Phi^-\rangle$, with the fidelity of 93.45%, 96.86%, 96.34%, and 94.58%, respectively. This approach significantly reduces the number of conventional optical components in the QST process.

First, we schematically show that two identical combined metasurfaces (MS1 and MS2), each possessing four districts with different optical responses (Fig. 1), can perform QST on the polarization-entangled states. In Fig. 1, MS1–1, MS1–2, MS1–3, and MS1–4 play the role of horizontal ($|H\rangle$), vertical ($|V\rangle$), antidiagonal ($|A\rangle$), and right-handed circularly ($|R\rangle$) polarizers, respectively. The unit cell of each district is constructed with two nanopillars with different geometrical sizes and orientations. The interference of the radiations from the nanopillars leads to one zeroth output, projecting the input state onto a specific polarization state, such as LP or CP state. Suppose a single photon with an arbitrary polarization state shines on one of the four districts on the metasurface sequentially. In other words, the input polarization state is projected to four polarization projection bases $\hat{\mu}_i$ $(i = 1,2,3,4)$ with $\hat{\mu}_1 = |H\rangle\langle H|$, $\hat{\mu}_2 = |V\rangle\langle V|$, $\hat{\mu}_3 = |A\rangle\langle A|$, $\hat{\mu}_4 = |R\rangle\langle R|$, respectively. By measuring the output strength on different projection bases, it is possible to recover the polarization, phase, and amplitude of the single-photon state. When the input state becomes the unknown two-photon polarization-entangled state, the quantum

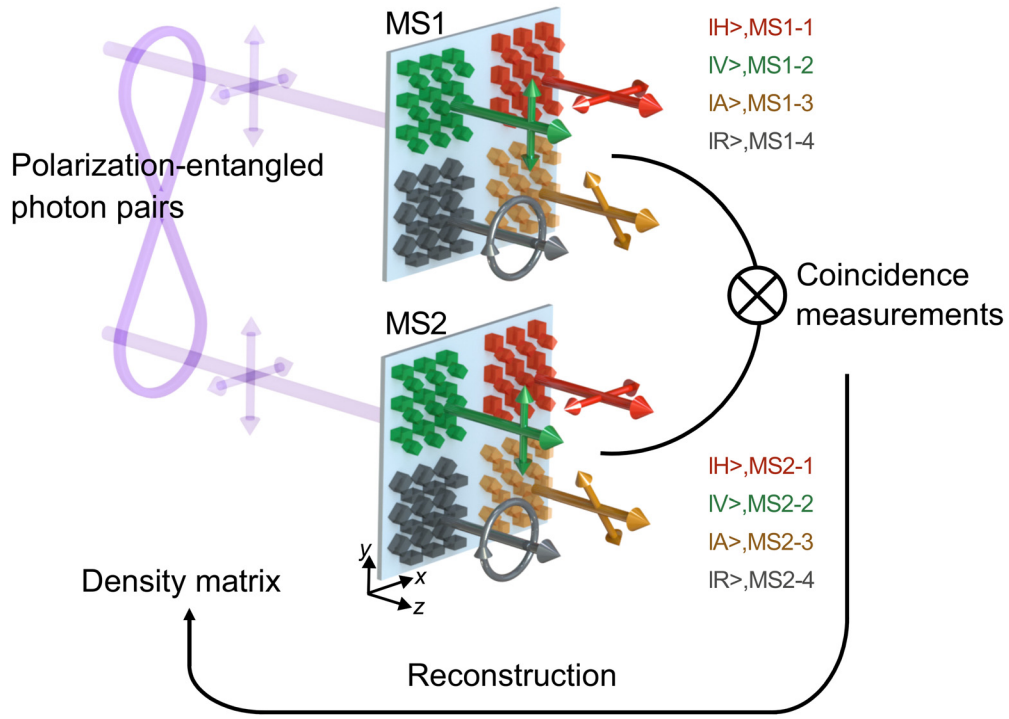

FIG. 1. Schematics showing two identical combined metasurfaces used for QST on the polarization-entangled states. Each metasurface is made of four districts with different optical responses. The unit cell of each district is constructed with two nanopillars with different geometrical sizes and orientation angles. Each district of the metasurface plays the role of horizontal ($|H\rangle$, red component), vertical ($|V\rangle$, green component), antidiagonal ($|A\rangle$, yellow component), and right-handed circularly ($|R\rangle$, gray component) polarizers. By allowing the polarization-entangled photon pairs to pass through different districts of the metasurfaces, we carry out coincidence measurements with two single-photon counting modules (SPCMs) to reconstruct the density matrix of the quantum state via a maximum likelihood estimation algorithm.

state can be reconstructed with two identical metasurfaces, MS1 and MS2. Suppose an entangled photon pair shines on different districts of the metasurfaces MS1 and MS2. The entangled state will be projected to $\hat{\mu}_i$ and $\hat{\mu}_j$ simultaneously ($i, j = 1,2,3,4$). The set of measurements $\hat{\mu}_i \otimes \hat{\mu}_j$ is tomographically complete. Thus, there are 16 projection bases. By executing coincidence measurements of two single-photon counting modules (SPCMs) with single-mode optical fiber, we can reconstruct the density matrix of the arbitrary polarization-entangled state using the maximum likelihood estimation algorithm and then calculate the fidelity of the incident photon state. The fidelity is defined

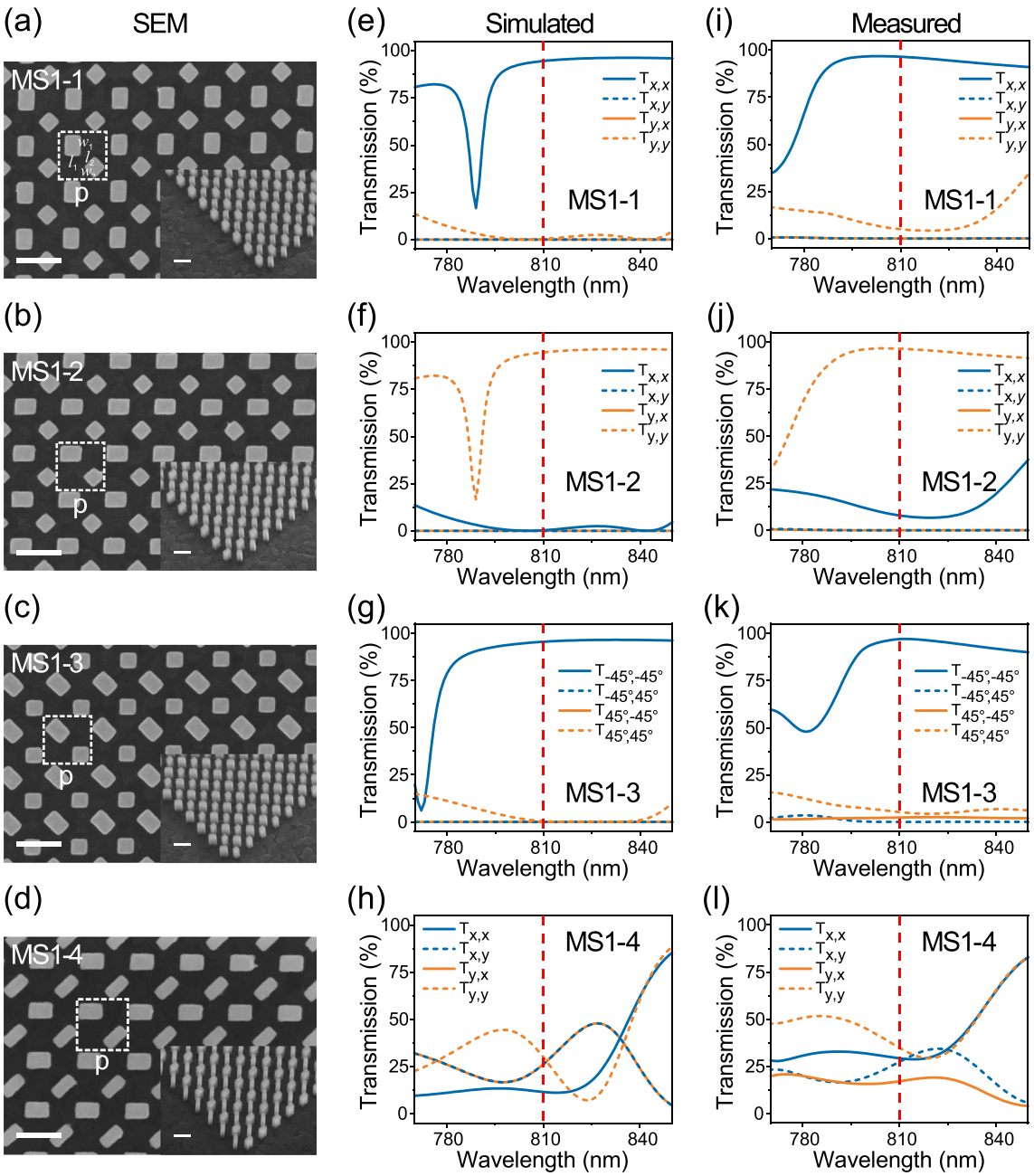

FIG. 2. SEM and transmission spectra of the fabricated metasurface. (a)–(d) SEM micrograph of the fabricated dielectric metasurface (MS1) in four districts (MS1-1, MS1-2, MS1-3, and MS1-4). The dashed line box represents the unit cell of each district. The inset is the oblique view of four districts. The white bars all represent 400 nm. (e)–(h) Simulated transmission spectra and (i)–(l) experimentally measured transmission spectra of MS1-1, MS1-2, MS1-3, and MS1-4, respectively. The wavelength ranges from 770 to 850 nm. $T_{\gamma,\delta}$ represents the δ-polarized component of the transmission coefficient under γ-polarized incidence.

as $F(\rho,\tilde{\rho}) = Tr\left(\sqrt{\tilde{\rho}^{\frac{1}{2}}\rho\tilde{\rho}^{\frac{1}{2}}}\right)^2$ to characterize the quality of the quantum state,[62] where ρ and $\tilde{\rho}$ are the theoretical and reconstructed density matrices, respectively. The near-unity fidelity indicates that the entangled state is close to the theoretical one.

Now, we consider the interaction of light with the periodic array of silicon nanopillars. Suppose the unit cell is made of N nanopillars along the x-axis. The interference of the radiations from the silicon nanopillars generates the desired output beams. The process can be described by the superposition of N Jones matrices as

$$\hat{J}_m = \frac{\sin(m\pi/N)}{m\pi}\sum_{j=1}^{N} e^{-i\frac{2\pi mj}{N}} R(-\theta_j)\begin{bmatrix} e^{i\phi_{xj}} & 0 \\ 0 & e^{i\phi_{yj}} \end{bmatrix} R(\theta_j), \quad (1)$$

where m is the diffraction order, N is the number of nanopillars in the unit cell, θ_j is the rotation angle of the nanopillar to the x-axis, $R(\theta_j)$ is the rotation matrix with the form $R(\theta_j) = \begin{bmatrix} \cos\theta_j & \sin\theta_j \\ -\sin\theta_j & \cos\theta_j \end{bmatrix}$, and ϕ_{xj} and ϕ_{yj} represent the GSI phase determined by the structural parameters when the incidence is polarized along two symmetrical axes of the nanopillar in the x–y plane,[27] respectively. In our current system, we choose $N = 2$ and the period p, which is smaller than the wavelength for the existence of only zeroth diffraction ($m = 0$).[19] Furthermore, we carefully design the geometrical size and the rotation angle of the nanopillars to maximize the transmission efficiency (the ratio of the intensity of the zero-order beam and that of the incident beam). It follows that the first nanopillar satisfies $\phi_{x1} = 0$, $\phi_{y1} = \pi$, and the orientation angle is θ_1, while the second nanopillar satisfied $\phi_{x2} = -\phi_{y2}$ and the orientation angle is $\left(\theta_1 - \frac{\pi}{4}\right)$.

Next step, by elaborately selecting θ_1 and ϕ_{y2}, each district in the metasurface could play the role of the desired polarizer. We carefully select the structural parameters of the silicon nanopillars with the finite-difference time-domain (FDTD) simulation. Suppose that two silicon nanopillars in the unit cell locate at $(-p/4, p/4)$ and $(p/4, -p/4)$, respectively, and they have the same height of 400 nm. The lengths in the x–y plane and the rotation angle of the first (second) nanopillar are, respectively, l_1, w_1, θ_1 [l_2, w_2, $\left(\theta_1 - \frac{\pi}{4}\right)$]. When the incident light with a wavelength ranging from 770 to 850 nm propagates in the z-direction, four polarization states $\hat{\mu}_i$ ($i = 1,2,3,4$) can be achieved from the following four districts in the metasurface. (i) $\hat{\mu}_1 = |H\rangle\langle H|$ comes from MS1–1, as illustrated in Fig. 2(a). We assume that $T_{\gamma,\delta}$ represents the δ-polarized component of the transmission coefficient for γ-polarized incidence. In this case, $T_{x,x}$ is close to 95% [the solid blue line of Fig. 2(e)], and the sum of $T_{y,x}$ and $T_{y,y}$ nearly vanishes [the orange dashed and solid lines in Fig. 2(e)] at 810 nm. (ii) $\hat{\mu}_2 = |V\rangle\langle V|$ comes from MS1–2, as illustrated in Fig. 2(b). Figure 2(f) shows that $T_{y,y}$ is close to 95% [the orange dashed line in Fig. 2(f)], and the sum of $T_{x,x}$ and $T_{x,y}$ approaches zero [the blue dashed and solid lines in Fig. 2(f)] at 810 nm. (iii) $\hat{\mu}_3 = |A\rangle\langle A|$ comes from MS1–3, as illustrated in Fig. 2(c). Figure 2(g) shows that $T_{-45^\circ,-45^\circ}$ is higher than 95% [the solid blue line in Fig. 2(g)], and the sum of $T_{45^\circ,-45^\circ}$ and $T_{45^\circ,45^\circ}$ vanishes [the orange dashed and solid lines in Fig. 2(g)] at 810 nm. (iv) $\hat{\mu}_4 = |R\rangle\langle R|$ comes from MS1–4, as illustrated in Fig. 2(d). As shown in Fig. 2(h), $T_{x,x}$, $T_{x,y}$, $T_{y,x}$, and $T_{y,y}$ are nearly identical at 810 nm. The nearly equal x- and y-components and the 90° phase difference between x- and y-components of the transmission coefficient indicate that the transmitted light is in CP state for both x- and y-polarized incidence. When the x-polarized, y-polarized, −45°-polarized, and RCP light incidents on MS1–1, MS1–2, MS1–3, and MS1–4, respectively, the transmission efficiency is accordingly 95%, 95%, 95%, and 94%, respectively. The transmission efficiency in each district is above 94%. We want to emphasize that the metasurface design differs from that in Ref. 43. The simulation results show that upon normal incidence, each district of the metasurface allows the nondiffractive transmission of the specific polarization state (such as CP and LP) with high efficiency.

To fabricate the silicon metasurface, we deposit a layer of 400 nm thick amorphous silicon on a cleaned indium tin oxide/glass substrate by plasma-enhanced chemical vapor deposition (PECVD). Then, on the top of the silicon layer, an array of the Al_2O_3 pattern of the nanopillars is formed by electron beam lithography, electron beam evaporation, and lift-off techniques. After that, dry etching of amorphous silicon is performed with a mixture of SF_6 and C_4F_8 with the Al_2O_3 pattern as the hard mask. Finally, the silicon nanopillars are fabricated. The size of each district of the metasurface is $350 \times 350\ \mu m^2$. The scanning electron micrographs (SEM) of the fabricated nanopillars in four different districts are shown in Figs. 2(a)–2(d), respectively.

The transmission spectra of four districts in metasurface with the wavelength ranging from 770 to 850 nm are experimentally measured with a UV-visible-near-infrared micro-spectrometer, as illustrated in Figs. 2(i)–2(l). At the wavelength of 810 nm, for MS1–1, $T_{x,x}$ reaches 96% [the solid blue line in Fig. 2(i)]; for MS1–2, $T_{y,y}$ reaches 96% [the orange dashed line in Fig. 2(j)]; for MS1–3, $T_{-45^\circ,-45^\circ}$ reaches 97% [the solid blue line in Fig. 2(k)]; for MS1–4, $T_{x,x}$, $T_{x,y}$, $T_{y,x}$, and $T_{y,y}$ are nearly identical [as shown in Fig. 2(l)], and the phase differences between x and y components under x- and y-polarized incidence are 92° and 97°, respectively. This indicates that the transmitted light is in a CP state. The measured results of four districts are in good agreement with the simulated ones [Figs. 2(e)–2(h)]. Moreover, when the x-polarized, y-polarized, −45°-polarized, and RCP light incidents on MS1–1, MS1–2, MS1–3, and MS1–4, respectively, the measured transmission efficiency at each district is above 92%. Each district of the metasurface allows a specific polarization state (such as CP or LP) with high efficiency to pass through.

Furthermore, we verify that metasurface can act as polarizers with a single-photon source at wavelength 810 nm. The key component of the single-photon source is a periodically poled potassium titanyl phosphate (PPKTP) crystal embedded in the Sagnac interferometer,[63] which is pumped by a 405 nm continuous-wave (CW) laser. First, the polarization-entangled photon pairs at 810 nm are generated through the spontaneous parametric down-conversion (SPDC) process in PPKTP. Then, the down-converted entangled photon pairs are

TABLE I. The measured extinction ratio of each district (MS1-1, MS1-2, MS1-3, and MS1-4).

Districts	Input photon states (α and β)	Extinction ratio (T_α/T_β)
MS1-1	Horizontally and vertically LP	254:1
MS1-2	Vertically and horizontally LP	56:1
MS1-3	−45° and 45° LP	226:1
MS1-4	Right-handed and left-handed CP	43:1

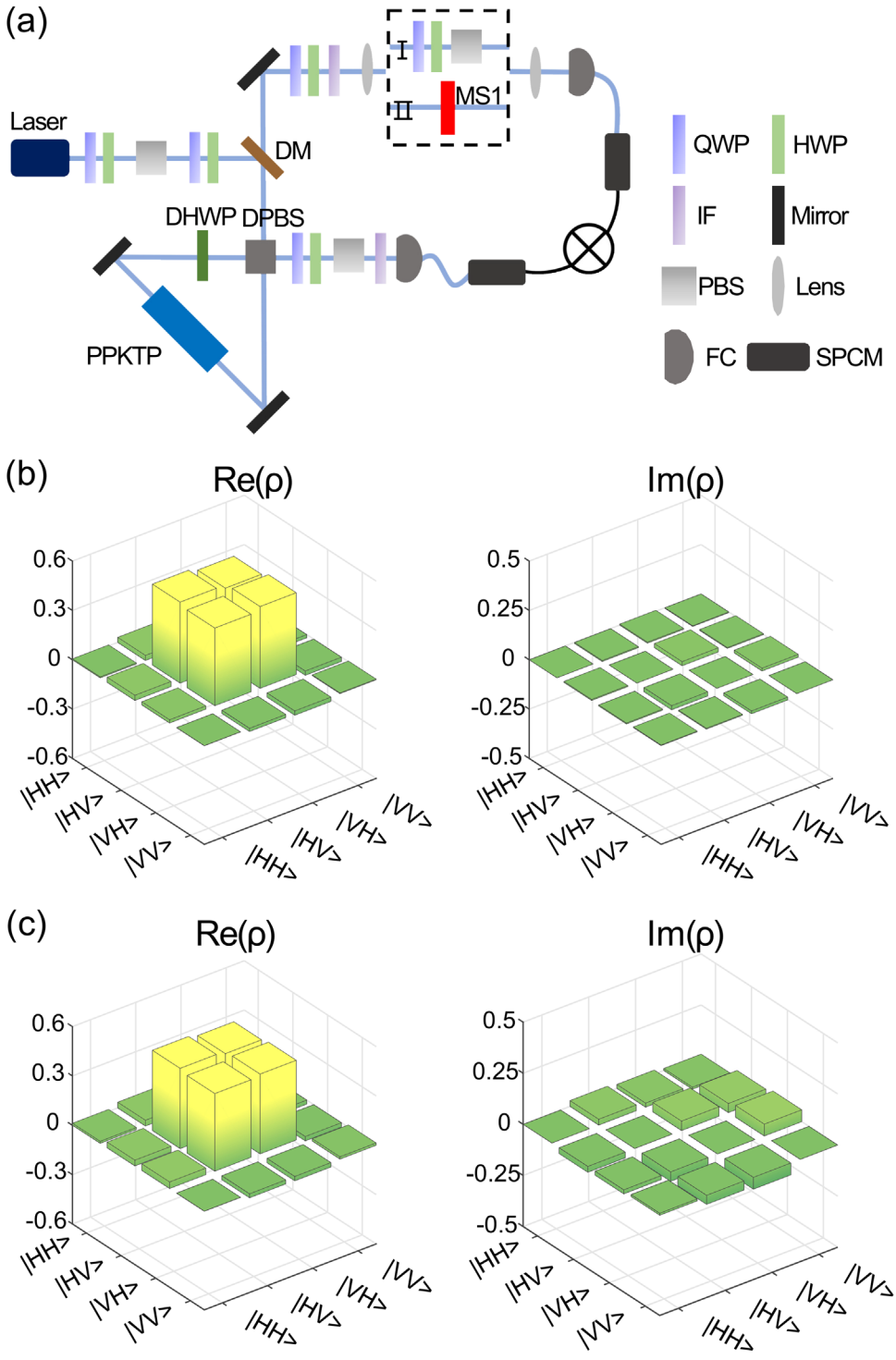

FIG. 3. The experiment to achieve QST by replacing traditional optical elements in one arm of the routes with MS1. (a) Schematics of the experimental setup. DHWP: dual-wavelength (405 and 810 nm) half-wave plate; DM: dichroism mirror; IF: interference filter; FC: fiber coupler. A 405 nm CW laser pumps PPKTP crystal to generate 810 nm polarization-entangled photon pairs through the SPDC process. One of the photon pairs passes through QWP, HWP, and PBS. Another photon passes through either the QWP, HWP, and PBS (route I) or four distinct regions of MS1 (route II) to project the input state on different polarization bases for QST. (b) and (c) The measured real and imaginary parts of density matrices for the input entangled state $|\Psi^+\rangle = \frac{1}{\sqrt{2}}(|H\rangle|V\rangle + |V\rangle|H\rangle)$ based on: (b) route I and (c) route II, respectively. The measured fidelities are 96.70% and 95.87%, respectively.

spatially separated. The photon in one arm passes through a different district of MS1 and projects the quantum state on a specific polarization state. We define the extinction ratio as the ratio of the photon counts T_α/T_β when the input photon states are, respectively, α and β. The measured extinction ratio of each district (MS1–1, MS1–2, MS1–3, and MS1–4) is listed in Table I. For MS1–1, α and β are horizontally and vertically LP, respectively; for MS1–2, α and β are vertically and horizontally LP, respectively; for MS1–3, α and β are -45°

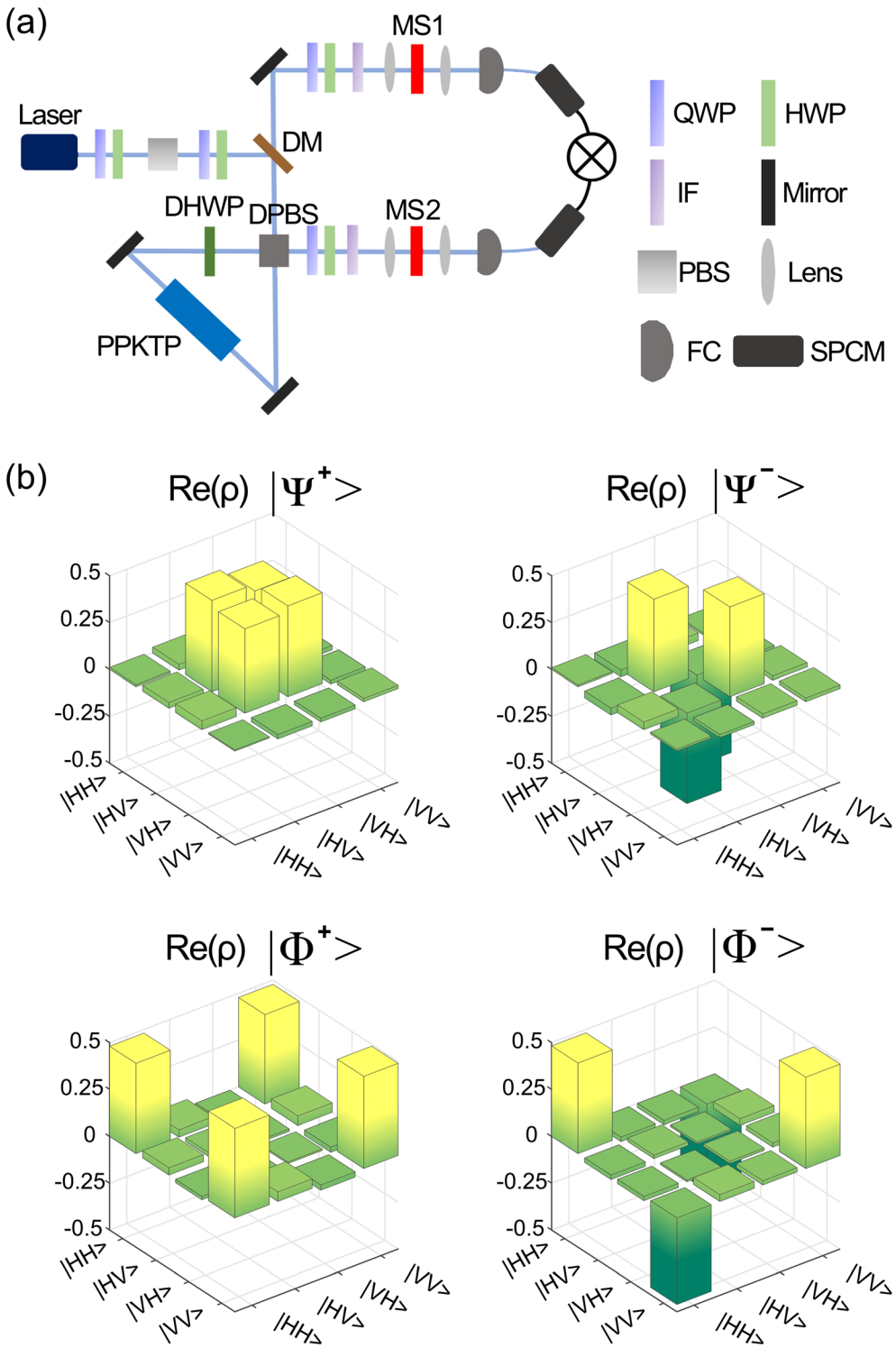

FIG. 4. Experiments to characterize QST with metasurfaces only. (a) Schematics of the experimental setup. DHWP: dual-wavelength (405 and 810 nm) half-wave plate; DM: dichroism mirror; IF: interference filter; FC: fiber coupler. The down-converted photon pairs are spatially separated via DPBS and pass through MS1 and MS2. (b) Experimentally measured real parts of density matrices for four input Bell states based on metasurfaces. The fidelities of $|\Psi^+\rangle$, $|\Psi^-\rangle$, $|\Phi^+\rangle$, and $|\Phi^-\rangle$ reach 93.45%, 96.86%, 96.34%, and 94.58%, respectively. The imaginary parts of density matrices for four Bell states have nearly vanished.

and 45° LP, respectively; for MS1–4, α and β are right-handed and left-handed CP, respectively. Therefore, one may find that the extinction ratio characterizes the performance of each district functioning as a polarizer. For the ideal situation, this ratio should be infinity. The high ratio characterizes that the district behaves as a perfect polarizer. From Table I, it can be seen that the maximum extinction ratio is 254, and the minimum extinction ratio is 43. Moreover, to characterize the loss of MS1, we define the efficiency of each district as the ratio of the photon counts T_α/T_{ref}. Here, T_{ref} is the photon counts when the input photon passes through the substrate. The measured efficiency of MS1–1, MS1–2, MS1–3, and MS1–4 is 96%, 97%, 94%, and 96%, respectively. The results are consistent with those shown in Fig. 2.

To carry out QST with metasurface, we put MS1 in one arm of the entangled source (black dashed line), as illustrated in Fig. 3(a). An arbitrary entangled state (the input state) can be achieved by modulating QWP and HWP before the interference filter (IF). The down-converted polarization-entangled photon pairs with the wavelength of 810 nm are separated by a dual-wavelength polarization beam splitter (DPBS). One photon of the photon pair passes through the combination of QWP, HWP, and PBS, and the single-photon state is projected onto a specific polarization. Meanwhile, another photon passes through either the QWP, HWP, and PBS (route I, with traditional optical elements) or four distinct regions of MS1 (route II, with metasurface). By shifting the metasurface districts with a three-axis translation stage or rotating the QWP and HWP, the input two-photon state is projected onto 16 polarization bases. By counting the coincidence counts between two SPCMs in 5s with the coincidence window of 1.5 ns from 16 different measurements ($\hat{\mu}_i \otimes \hat{\mu}_j$) for entangled photons, we can reconstruct the density matrix of unknown polarization-entangled photons.

Suppose the incident state is the Bell state $|\Psi^+\rangle = \frac{1}{\sqrt{2}}(|H\rangle|V\rangle + |V\rangle|H\rangle)$. We carry out full QST on this input state. With 16 different measurements, we reconstruct a two-photon density matrix based on traditional optical elements QWP, HWP, and PBS (route I). As illustrated in Fig. 3(b), the fidelity of the quantum source is 96.70%. Then, we change to route II, i.e., replacing the traditional optical elements with MS1. The entangled photons pass through the four distinct regions of MS1 to project the quantum state on different polarization bases. We acquire coincidence counts from 16 measurements. Figure 3(c) shows the experimentally reconstructed density matrix of $|\Psi^+\rangle$ based on MS1 with the fidelity of 95.87%, and the slightly lower fidelity here may be due to the imperfection in the fabrication of the metasurface.

We have confirmed in Fig. 3 that the metasurface can replace part of traditional optical elements for QST. Now, we perform QST solely with two identical metasurfaces, MS1 and MS2, as shown in Fig. 4(a). By rotating QWP and HWP in front of the IF, any of the four Bell states ($|\Psi^\pm\rangle = \frac{1}{\sqrt{2}}(|H\rangle|V\rangle \pm |V\rangle|H\rangle)$ and ($|\Phi^\pm\rangle = \frac{1}{\sqrt{2}}(|H\rangle|H\rangle \pm |V\rangle|V\rangle)$) can be generated as the input state. By shifting the metasurface on a 3-axis translation stage, each district on the metasurface will interact with the incident entangled photon. For each incident Bell state, 16 two-photon coincidence counts are measured, and the density matrices are reconstructed with the maximum likelihood estimation method, as illustrated in Fig. 4(b). The measured fidelities of four Bell states $|\Psi^+\rangle$, $|\Psi^-\rangle$, $|\Phi^+\rangle$, and $|\Phi^-\rangle$ are 93.45%, 96.86%, 96.34%, and 94.58%, respectively. When QST is measured with traditional optical elements (QWP, HWP, and PBS), the fidelities are 96.70%, 97.44%, 98.13%, and 97.55%. The fidelities measured by metasurfaces are comparable with those acquired from the traditional optical elements, which confirm the effectiveness of using metasurfaces in the QST process.

Generally speaking, to characterize Q-photon polarization-entangled state with the current QST technology, $3Q$ pieces of bulky optical components, including QWP, HWP, and PBS, are required. However, with the approach presented in this work, Q pieces of metasurfaces are sufficient to accomplish the characterization. This approach significantly reduces the number of traditional optical components in experiments. Here, we experimentally demonstrate the QST of the two-photon polarization-entangled state with two pieces of metasurfaces. The measured results with metasurfaces, such as density matrix and fidelity, can be almost identical to that of traditional optical components when the fabricated nanopillar possesses sharper edges and more accurate geometrical sizes with an improved nanofabrication process. Meanwhile, the loss of dielectric metasurfaces is very limited, and currently, the measured efficiency of silicon metasurfaces reaches an average of 96%, which is practically applicable to nowadays quantum measurement configurations. Furthermore, if the metasurfaces are upgraded from the passive to the active one,[48] shifting different metasurface districts for the state projection by the 3-axis translation stage may become unnecessary. This will benefit further miniaturization of the photonic platform for quantum information processing.

To conclude, this work demonstrates that QST can be accomplished with nondiffractive silicon metasurfaces without using traditional waveplates and polarization beam splitters. Due to phase modulation at the subwavelength scale, the metasurfaces enable the nondiffractive output with the projection of the multiphoton state onto various polarization bases with high efficiency. The experimental reconstruction of the density matrices of four different input Bell states, $|\Psi^\pm\rangle$ and $|\Phi^\pm\rangle$, with the fidelity of 93.45%, 96.86%, 96.34%, and 94.58% indicates that metasurfaces are qualified to measure the quantum states. This strategy significantly reduces the number of traditional optical components in quantum measurement and is promising for developing quantum information processing.

This work was supported by the National Key R&D Program of China (Nos. 2020YFA0211300 and 2017YFA0303702), the National Natural Science Foundation of China (Grant Nos. 61975078 and 11974177), the China National Postdoctoral Program for Innovative Talents (No. BX20220146), and the Jiangsu Funding Program for Excellent Postdoctoral Talent (No. 20220ZB3).

AUTHOR DECLARATIONS

Conflict of Interest

The authors have no conflicts to disclose.

Author Contributions

Z.W., Y.J., and Y.-J.G. contributed equally to this work.
Zheng Wang: Formal analysis (equal); Investigation (equal); Writing – original draft (equal). **Yue Jiang:** Formal analysis (equal); Investigation (equal). **Ya-Jun Gao:** Formal analysis (equal); Investigation (equal); Writing – original draft (equal). **Ren-Hao Fan:** Formal analysis

(equal). **Dong-Xiang Qi:** Formal analysis (equal). **Rui Zhong:** Formal analysis (equal). **Hu-Lin Zhang:** Formal analysis (equal). **Ru-Wen Peng:** Conceptualization (equal); Investigation (equal); Supervision (equal); Writing – original draft (equal). **Mu Wang:** Conceptualization (equal); Investigation (equal); Supervision (equal); Writing – original draft (equal).

DATA AVAILABILITY

The data that support the findings of this study are available from the corresponding authors upon reasonable request.

REFERENCES

[1]N. Yu, P. Genevet, M. A. Kats, F. Aieta, J.-P. Tetienne, F. Capasso, and Z. Gaburro, Science **334**, 333 (2011).
[2]X. Li, L. Chen, Y. Li, X. Zhang, M. Pu, Z. Zhao, X. Ma, Y. Wang, M. Hong, and X. Luo, Sci. Adv. **2**, e1601102 (2016).
[3]Z. Zhou, J. Li, R. Su, B. Yao, H. Fang, K. Li, L. Zhou, J. Liu, D. Stellinga, C. P. Reardon, T. F. Krauss, and X. Wang, ACS Photonics **4**, 544 (2017).
[4]S. Wang, P. C. Wu, V.-C. Su, Y.-C. Lai, M.-K. Chen, H. Y. Kuo, B. H. Chen, Y. H. Chen, T.-T. Huang, J.-H. Wang, R.-M. Lin, C.-H. Kuan, T. Li, Z. Wang, S. Zhu, and D. P. Tsai, Nat. Nanotechnol. **13**, 227 (2018).
[5]R. Zhao, B. Sain, Q. Wei, C. Tang, X. Li, T. Weiss, L. Huang, Y. Wang, and T. Zentgraf, Light: Sci. Appl. **7**, 95 (2018).
[6]R. H. Fan, B. Xiong, R. W. Peng, and M. Wang, Adv. Mater. **32**, 1904646 (2020).
[7]Y. Bao, J. Ni, and C.-W. Qiu, Adv. Mater. **32**, 1905659 (2020).
[8]Z.-L. Deng, M. Jin, X. Ye, S. Wang, T. Shi, J. Deng, N. Mao, Y. Cao, B.-O. Guan, A. Alù, G. Li, and X. Li, Adv. Funct. Mater. **30**, 1910610 (2020).
[9]B. Xiong, Y. Xu, J. Wang, L. Li, L. Deng, F. Cheng, R.-W. Peng, M. Wang, and Y. Liu, Adv. Mater. **33**, 2005864 (2021).
[10]Y. Wang, Q. Chen, W. Yang, Z. Ji, L. Jin, X. Ma, Q. Song, A. Boltasseva, J. Han, V. M. Shalaev, and S. Xiao, Nat. Commun. **12**, 5560 (2021).
[11]W. Ye, X. Yuan, C. Guo, J. Zhang, B. Yang, and S. Zhang, Phys. Rev. Appl. **7**, 054003 (2017).
[12]S.-C. Jiang, X. Xiong, Y.-S. Hu, Y.-H. Hu, G.-B. Ma, R.-W. Peng, C. Sun, and M. Wang, Phys. Rev. X **4**, 021026 (2014).
[13]R.-H. Fan, Y. Zhou, X.-P. Ren, R.-W. Peng, S.-C. Jiang, D.-H. Xu, X. Xiong, X.-R. Huang, and M. Wang, Adv. Mater. **27**, 1201 (2015).
[14]A. Arbabi, Y. Horie, M. Bagheri, and A. Faraon, Nat. Nanotechnol. **10**, 937 (2015).
[15]M. Jia, Z. Wang, H. Li, X. Wang, W. Luo, S. Sun, Y. Zhang, Q. He, and L. Zhou, Light.: Sci. Appl. **8**, 16 (2019).
[16]Q. Ma, Q. R. Hong, G. D. Bai, H. B. Jing, R. Y. Wu, L. Bao, Q. Cheng, and T. J. Cui, Phys. Rev. Appl. **13**, 021003 (2020).
[17]Y. Yuan, K. Zhang, B. Ratni, Q. Song, X. Ding, Q. Wu, S. N. Burokur, and P. Genevet, Nat. Commun. **11**, 4186 (2020).
[18]H. Kwon, E. Arbabi, S. M. Kamali, M. Faraji-Dana, and A. Faraon, Nat. Photonics **14**, 109 (2020).
[19]S. Wang, Z.-L. Deng, Y. Wang, Q. Zhou, X. Wang, Y. Cao, B.-O. Guan, S. Xiao, and X. Li, Light. Sci. Appl. **10**, 24 (2021).
[20]S. Gao, C. Zhou, W. Liu, W. Yue, S. Chen, S.-S. Lee, D.-Y. Choi, and Y. Li, Laser Photonics Rev. **16**, 2100603 (2022).
[21]D. Lin, P. Fan, E. Hasman, and M. L. Brongersma, Science **345**, 298 (2014).
[22]M. Khorasaninejad and K. B. Crozier, Nat. Commun. **5**, 5386 (2014).
[23]M. Khorasaninejad, W. T. Chen, R. C. Devlin, J. Oh, A. Y. Zhu, and F. Capasso, Science **352**, 1190 (2016).
[24]J. Li, S. Kamin, G. Zheng, F. Neubrech, S. Zhang, and N. Liu, Sci. Adv. **4**, eaar6768 (2018).
[25]Y. Ming, Y. Intaravanne, H. Ahmed, M. Kenney, Y. Lu, and X. Chen, Adv. Mater. **34**, 2109714 (2022).
[26]Y.-J. Gao, X. Xiong, Z. Wang, F. Chen, R.-W. Peng, and M. Wang, Phys. Rev. X **10**, 031035 (2020).
[27]Y.-J. Gao, Z. Wang, W. Tang, X. Xiong, Z. Wang, F. Chen, R.-W. Peng, and M. Wang, Phys. Rev. B **104**, 125419 (2021).
[28]J. P. B. Mueller, N. A. Rubin, R. C. Devlin, B. Groever, and F. Capasso, Phys. Rev. Lett. **118**, 113901 (2017).
[29]Q. Fan, M. Liu, C. Zhang, W. Zhu, Y. Wang, P. Lin, F. Yan, L. Chen, H. J. Lezec, Y. Lu, A. Agrawal, and T. Xu, Phys. Rev. Lett. **125**, 267402 (2020).
[30]E. Altewischer, M. P. van Exter, and J. P. Woerdman, Nature **418**, 304 (2002).
[31]T. Roger, S. Vezzoli, E. Bolduc, J. Valente, J. J. F. Heitz, J. Jeffers, C. Soci, J. Leach, C. Couteau, N. I. Zheludev, and D. Faccio, Nat. Commun. **6**, 7031 (2015).
[32]P. K. Jha, X. Ni, C. Wu, Y. Wang, and X. Zhang, Phys. Rev. Lett. **115**, 025501 (2015).
[33]S. Chen, X. Zhou, C. Mi, Z. Liu, H. Luo, and S. Wen, Appl. Phys. Lett. **110**, 161115 (2017).
[34]C. Altuzarra, S. Vezzoli, J. Valente, W. Gao, C. Soci, D. Faccio, and C. Couteau, ACS Photonics **4**, 2124 (2017).
[35]P. K. Jha, N. Shitrit, J. Kim, X. Ren, Y. Wang, and X. Zhang, ACS Photonics **5**, 971 (2018).
[36]A. Lyons, D. Oren, T. Roger, V. Savinov, J. Valente, S. Vezzoli, N. I. Zheludev, M. Segev, and D. Faccio, Phys. Rev. A **99**, 011801 (2019).
[37]L. Li, Z. Liu, X. Ren, S. Wang, V.-C. Su, M.-K. Chen, C. H. Chu, H. Y. Kuo, B. Liu, W. Zang, G. Guo, L. Zhang, Z. Wang, S. Zhu, and D. P. Tsai, Science **368**, 1487 (2020).
[38]Y.-Y. Xie, P.-N. Ni, Q.-H. Wang, Q. Kan, G. Briere, P.-P. Chen, Z.-Z. Zhao, A. Delga, H.-R. Ren, H.-D. Chen, C. Xu, and P. Genevet, Nat. Nanotechnol. **15**, 125 (2020).
[39]Y. Kan, S. K. H. Andersen, F. Ding, S. Kumar, C. Zhao, and S. I. Bozhevolnyi, Adv. Mater. **32**, 1907832 (2020).
[40]A. S. Solntsev, G. S. Agarwal, and Y. S. Kivshar, Nat. Photonics **15**, 327 (2021).
[41]J. Liu, M. Shi, Z. Chen, S. Wang, Z. Wang, and S. Zhu, Opto-Electron. Adv. **4**, 200092 (2021).
[42]Q.-Y. Wu, Z. Meng, J.-Z. Yang, and A.-N. Zhang, npj Quantum Inf. **8**, 46 (2022).
[43]K. Wang, J. G. Titchener, S. S. Kruk, L. Xu, H.-P. Chung, M. Parry, I. I. Kravchenko, Y.-H. Chen, A. S. Solntsev, Y. S. Kivshar, D. N. Neshev, and A. A. Sukhorukov, Science **361**, 1104 (2018).
[44]T. Stav, A. Faerman, E. Maguid, D. Oren, V. Kleiner, E. Hasman, and M. Segev, Science **361**, 1101 (2018).
[45]W. J. M. Kort-Kamp, A. K. Azad, and D. A. R. Dalvit, Phys. Rev. Lett. **127**, 043603 (2021).
[46]Q. Li, W. Bao, Z. Nie, Y. Xia, Y. Xue, Y. Wang, S. Yang, and X. Zhang, Nat. Photonics **15**, 267 (2021).
[47]H. Liang, K. M. Lau, W. C. Wong, S. Du, W. Y. Tam, and J. Li, Phys. Rev. A **104**, 063710 (2021).
[48]D. Zhang, Y. Chen, S. Gong, W. Wu, W. Cai, M. Ren, X. Ren, S. Zhang, G. Guo, and J. Xu, Light: Sci. Appl. **11**, 58 (2022).
[49]C. Altuzarra, A. Lyons, G. Yuan, C. Simpson, T. Roger, J. S. Ben-Benjamin, and D. Faccio, Phys. Rev. A **99**, 020101 (2019).
[50]P. Georgi, M. Massaro, K.-H. Luo, B. Sain, N. Montaut, H. Herrmann, T. Weiss, G. Li, C. Silberhorn, and T. Zentgraf, Light: Sci. Appl. **8**, 70 (2019).
[51]J. Zhou, S. Liu, H. Qian, Y. Li, H. Luo, S. Wen, Z. Zhou, G. Guo, B. Shi, and Z. Liu, Sci. Adv. **6**, eabc4385 (2020).
[52]A. Vega, T. Pertsch, F. Setzpfandt, and A. A. Sukhorukov, Phys. Rev. Appl. **16**, 064032 (2021).
[53]D. F. V. James, P. G. Kwiat, W. J. Munro, and A. G. White, Phys. Rev. A **64**, 052312 (2001).
[54]M. A. Nielsen and I. L. Chuang, *Quantum Computation and Quantum Information* (Cambridge University Press, 2002).
[55]M. Agnew, J. Leach, M. McLaren, F. S. Roux, and R. W. Boyd, Phys. Rev. A **84**, 062101 (2011).
[56]J. G. Titchener, M. Gräfe, R. Heilmann, A. S. Solntsev, A. Szameit, and A. A. Sukhorukov, npj Quantum Inf. **4**, 19 (2018).
[57]L.-C. Peng, D. Wu, H.-S. Zhong, Y.-H. Luo, Y. Li, Y. Hu, X. Jiang, M.-C. Chen, L. Li, N.-L. Liu, K. Nemoto, W. J. Munro, B. C. Sanders, C.-Y. Lu, and J.-W. Pan, Phys. Rev. Lett. **125**, 210502 (2020).
[58]E. Toninelli, B. Ndagano, A. Vallés, B. Sephton, I. Nape, A. Ambrosio, F. Capasso, M. J. Padgett, and A. Forbes, Adv. Opt. Photonics **11**, 67 (2019).

[59]K. J. Resch, P. Walther, and A. Zeilinger, Phys. Rev. Lett. **94**, 070402 (2005).
[60]W. Wieczorek, N. Kiesel, C. Schmid, and H. Weinfurter, Phys. Rev. A **79**, 022311 (2009).
[61]K. Banaszek, G. M. D'Ariano, M. G. A. Paris, and M. F. Sacchi, Phys. Rev. A **61**, 010304 (1999).
[62]R. Jozsa, J. Mod. Opt. **41**, 2315 (1994).
[63]Y. Li, Z.-Y. Zhou, D.-S. Ding, and B.-S. Shi, Opt. Express **23**, 28792 (2015).